Article

Broadband near-infrared hyperbolic polaritons in MoOCl$_2$

Yaolong Li [1,8] ✉, Yuxin Zhang[1,8], Weizhe Zhang[1], Xiaofang Li[1], Jinglin Tang[1], Jingying Xiao[1], Guanyu Zhang[1], Xin Liao [1], Pengzuo Jiang[1], Qinyun Liu[1], Yijie Luo[1], Zini Cao[1], Qinghong Lyu[1], Yuanbiao Tong[2], Ruoxue Yang[2], Hong Yang[1,3,4], Quan Sun [3], Yunan Gao [1,3,4], Pan Wang [2], Zuxin Chen [5], Wenjing Liu [1,3,4] ✉, Shufeng Wang [1,3,4] ✉, Guowei Lyu [1,3,4] ✉, Xiaoyong Hu [1,3,4,6] ✉, Martin Aeschlimann [7] ✉ & Qihuang Gong [1,3,4,6] ✉

Hyperbolic polaritons have drawn great attention in nanoscale light manipulation due to their unique properties. Currently, most studies focus on natural hyperbolic phonon materials in the mid-infrared, limiting their application in the visible to near-infrared range. Here, we present a work on broadband near-infrared hyperbolic plasmon polaritons in a van der Waals material MoOCl$_2$ by a perturbation-free direct imaging technique of photoemission electron microscopy. In particular, the hyperbolic polariton behavior has been dynamically tailored and manipulated by wavelength, polarization, interlayer twist, and artificial structure, providing a reconfigurable platform for nanophotonic applications. Notably, the full iso-frequency contours can be reconstructed via polarization-selective excitations. Our work has contributed to hyperbolic materials in the broadband near-infrared with MoOCl$_2$, and has revealed PEEM to be an ideal method for studying hyperbolic plasmon polaritons at the space-time limit.

In recent years, natural hyperbolic materials with opposite signs of permittivity along the two orthogonal directions supporting hyperbolic polaritons have attracted considerable attention. Due to their unusual optical properties, hyperbolic polaritons can produce many novel physical phenomena, such as deep subdiffractional field confinement and highly directional propagation, etc[1,2]. Hyperbolic phonon polaritons have been found in a few anisotropic van der Waals (vdW) materials and bulk crystals (e.g., hBN[3,4], α-MoO$_3$[5,6], α-V$_2$O$_5$[7] and calcite (CaCO$_3$)[8]) and have been intensively studied[9,10]. The phonon-assisted hyperbolic polaritons are typically located in the mid-infrared region,

due to the relatively low energy of phonons. This limits their potential applications in the near-infrared and visible ranges, which encompass the optical communications and on-chip information processing bands. To shorten the working wavelengths, collective exciton or electron resonances are considered to form exciton polaritons[11–13] or plasmon polaritons[14,15]. However, pushing the operating band into the near-infrared or visible region remains a challenge, due to the requirement of relatively high quasiparticle energy and strong anisotropy. Recently, an emerging class of layered vdW materials, MOX$_2$ (M = Nb, Ta, V, Mo, Ru; X = Cl, Br, I) has gained increasing attention due

[1]State Key Laboratory for Mesoscopic Physics & Department of Physics, Collaborative Innovation Center of Quantum Matter & Frontiers Science Center for Nano-optoelectronics, Peking University, Beijing, China. [2]State Key Laboratory of Extreme Photonics and Instrumentation, College of Optical Science and Engineering, Zhejiang University, Hangzhou, China. [3]Key Laboratory for Advanced Optoelectronic Integrated Chips of Jiangsu Province, Peking University Yangtze Delta Institute of Optoelectronics, Nantong, Jiangsu, China. [4]Collaborative Innovation Center of Extreme Optics, Shanxi University, Taiyuan, Shanxi, China. [5]School of Electronics Science & Engineering, South China Normal University, Foshan, China. [6]Hefei National Laboratory, Hefei, China. [7]Department of Physics and Research Center OPTIMAS, RPTU University Kaiserslautern-Landau, Kaiserslautern, Germany. [8]These authors contributed equally: Yaolong Li, Yuxin Zhang. ✉e-mail: yaolong@pku.edu.cn; wenjingl@pku.edu.cn; wangsf@pku.edu.cn; guowei.lu@pku.edu.cn; xiaoyonghu@pku.edu.cn; ma@physik.uni-kl.de; qhgong@pku.edu.cn

1

to the anisotropic crystal structure and unique physical properties, such as giant optical nonlinearity and in-plane optical anisotropy[16–21]. Among them, the highly anisotropic $MoOCl_2$ and $RuOCl_2$ are predicted to be promising candidates for supporting broadband hyperbolic plasmon polaritons in the visible to near-infrared range, with metallic ($\varepsilon_x < 0$) and dielectric ($\varepsilon_y > 0$) properties along two orthogonal in-plane directions and dielectric property in the out-of-plane direction ($\varepsilon_z > 0$)[16,17,21] (see Supplementary Table S1 for comparison with other materials), and the $MoOCl_2$ was recently experimentally investigated by scattering-type scanning near field optical microscope (s-SNOM)[22,23]. The experimental realization and manipulation of hyperbolic polaritons in the visible to near-infrared range will pave the way for innovative advances in nanophotonic applications.

For the experimental investigation of hyperbolic polaritons in the visible to near-infrared range, photoemission electron microscopy (PEEM) can be employed, as it offers significant advantages in the near-field imaging of polariton modes, allowing a comprehensive characterization of their properties. PEEM is ideal for obtaining perturbation-free and direct images of hyperbolic modes, and is capable of flexible polarization control at precisely normal incidence[24], which is crucial for direct observation of intrinsic near-field modes and dynamic manipulation. PEEM has been shown to be perfectly compatible with tunable femtosecond lasers, allowing convenient wavelength control and time-resolved measurements. This method has been successfully applied to the study of various near-field modes supported by metals and dielectrics, such as surface plasmon polaritons (SPPs)[24–30], localized surface plasmon resonances (LSPRs)[31–36] and planar dielectric waveguides[37–40], but the investigation in hyperbolic polaritons is still lacking.

In this work, we have revealed the $MoOCl_2$-assisted hyperbolic plasmon polaritons in the broadband near-infrared region (up to 1400 nm) using PEEM equipped with a tunable femtosecond laser with flexible polarization and wavelength control at normal incidence. Using gold nanoparticles as single-point excitation to launch hyperbolic polariton modes, we observed the transitions of modes with different wavelengths, polarizations, and interlayer twist angles. In particular, we observed the mode transition from hyperbolic plasmon polaritons to elliptical air modes with decreasing wavelength at

x-polarization, as well as a topological transition associated with twist angles. Importantly, polarization-selective excitations were observed in both real and k spaces, and the full iso-frequency contours (IFCs) can be reconstructed via polarization control. In addition, we demonstrated the feasibility of manipulating polaritons with artificial structures on $MoOCl_2$. Our study demonstrates that PEEM is a highly effective technique for imaging hyperbolic modes, offering notable advantages. It holds great potential for future applications in investigating near-field modes and their dynamics in vdW materials, particularly through time-resolved PEEM.

Results

Optical properties of $MoOCl_2$ and PEEM method

The crystal structure of each layer of the $MoOCl_2$ flake is shown in Fig. 1a, highlighting strong in-plane anisotropy (space group C2/m). The structure is strongly coupled along the Mo-O chains, while the inter-chain coupling in the orthogonal direction is significantly weaker. The measured permittivity is shown in Fig. 1b, with metallic ($\varepsilon_x < 0$) and dielectric ($\varepsilon_y > 0$) characters in the visible to near-infrared range along the two orthogonal directions, respectively (see Supplementary Note 3 for details of the permittivity measurements and Note 2 for comparison with other polariton materials). This anisotropy is also evident in the optical images of a representative sample taken with a reflective optical microscope (Fig. 1c), which show golden metallic luster and dielectric film color with polarizations along the x- and y-axes, respectively.

The hyperbolic plasmon polariton is determined by the measured permittivity, as confirmed in the representative finite-difference time-domain simulation. This simulation involves a tens of nm thick $MoOCl_2$ flake on glass, excited by an Au nanoparticle under normal light incidence (Fig. 1d).

To observe the broadband hyperbolic modes, we employed ultrahigh-spatial-resolution PEEM, integrated with a tunable femtosecond laser beamline (360–1800 nm). Unless otherwise specified, the light was incident at normal angles, with polarization controlled by a $\lambda/2$ waveplate. The schematic of the PEEM setup is illustrated in Fig. 1e. Near-field imaging in the near-infrared with PEEM relies on a multi-photon photoemission process to overcome the material's work
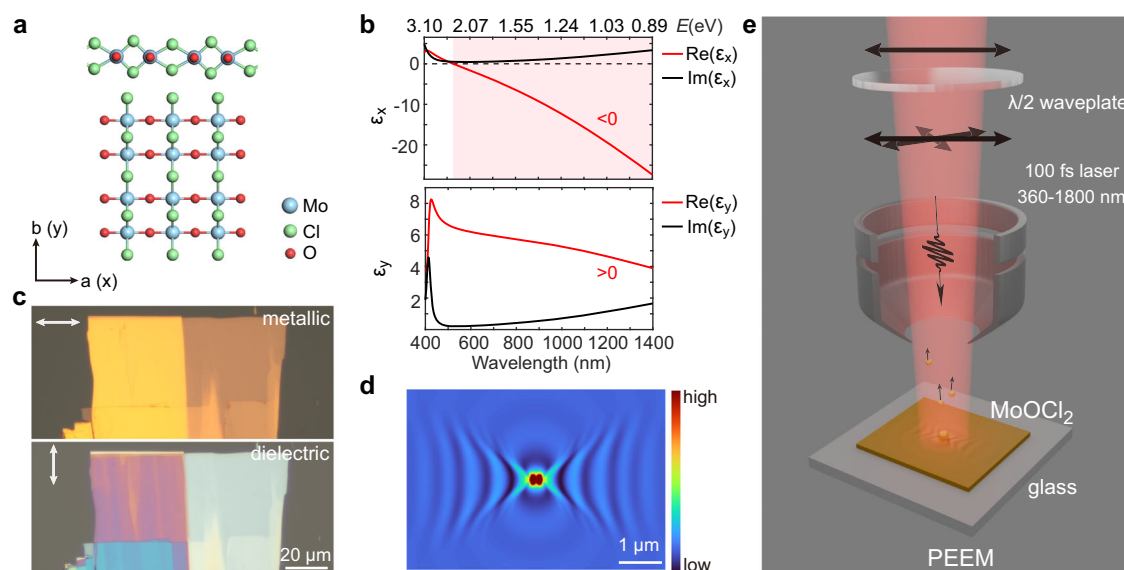

Fig. 1 | Broadband near-infrared hyperbolic plasmon polaritons in $MoOCl_2$ and PEEM method. a Crystal structure of each layer of the $MoOCl_2$ flake. The experimental coordinate axes (x, y) are along the crystal orientations (a, b), respectively. **b** Measured permittivity along the two orthogonal directions in the visible to near-infrared range. The light red shading indicates $Re(\varepsilon_x) < 0$. **c** Optical images of a representative sample taken with a reflective optical microscope at x- and y-

polarizations, showing golden metallic luster and dielectric film color, respectively. **d** Simulated hyperbolic plasmon polariton mode (electric field $|E|$) supported by a 40 nm $MoOCl_2$ flake on a glass substrate at 1000 nm wavelength, excited by an Au nanoparticle with x-polarization at normal incidence. **e** Schematic of PEEM measurements for near-field modes supported by $MoOCl_2$ flakes, allowing polarization and wavelength control at normal incidence.
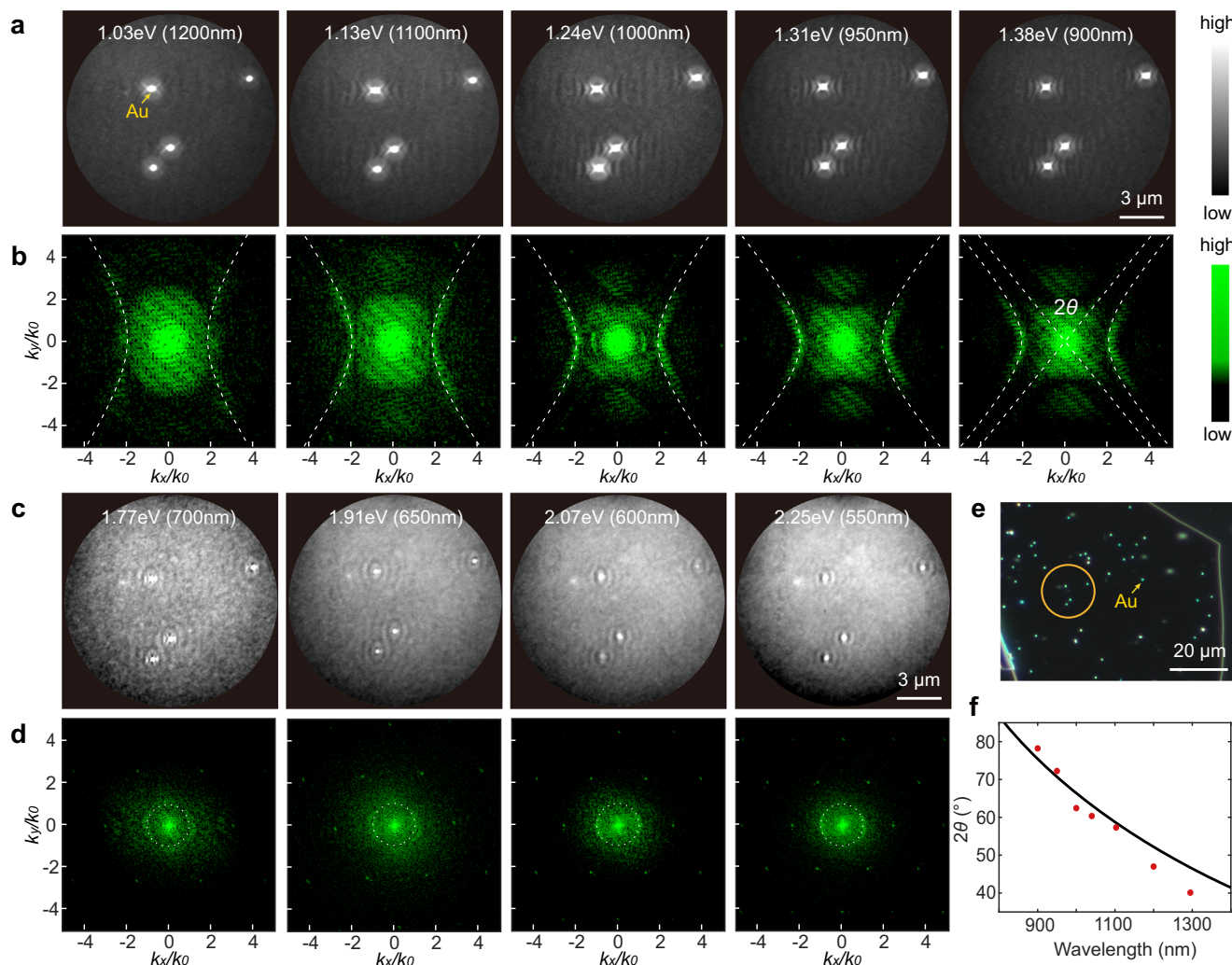
Fig. 2 | Wavelength-dependent near-field modes measured by PEEM with x-polarization at normal incidence. a Hyperbolic plasmon polariton modes from 1.03 eV (1200 nm) to 1.38 eV (900 nm) supported by a ~ 37 nm MoOCl$_2$ flake, excited from SiO$_2$-coated Au nanoparticles (5 nm SiO$_2$ @ 200 nm Au). **b** Corresponding iso-frequency contours (IFCs) (fast Fourier transform (FFT) of (**a**)), fitted with hyperbolas (white dashed lines). **c** Mode distributions at shorter wavelengths, from 1.77 eV (700 nm) to 2.25 eV (550 nm), showing the transition from hyperbolic mode to elliptical air mode. **d** Corresponding FFT images of (**c**). The white dashed cycles in (**d**) signify k_O. The color scales in (**a**, **b**) are also applied to (**c**, **d**). **e** Optical dark-field image of the measured sample, the yellow circle denotes the measured area by PEEM. **f** Variation of measured open angles (2θ) of hyperbolas in (**b**) with wavelengths (red dots), and the corresponding calculated curve from the measured permittivity.

function. In this study, a sub-monolayer of cesium (Cs) was deposited on all sample surfaces, lowering the work function to enable a two-photon photoemission process. The nonlinear photoemission yield follows $P_E \propto I^2$, where P_E is the photoemission intensity and I is the local light intensity (Supplementary Fig. 3, see also Supplementary Note 13 for more discussions on the PEEM method). Additionally, all PEEM measurements were conducted at ~ 85 K.

Wavelength-dependent mode distributions

A representative MoOCl$_2$ sample for PEEM studies is shown in Fig. 2e, with a thickness of ~ 37 nm. The MoOCl$_2$ flakes were mechanically exfoliated and transferred onto a glass substrate, coated with a thin (~ 10 nm) ITO layer to avoid surface charging during the PEEM experiments. SiO$_2$-coated Au nanoparticles (5 nm SiO$_2$ @ 200 nm Au) placed on top of the MoOCl$_2$ flakes served as couplers to excite hyperbolic plasmon polariton modes in MoOCl$_2$ (see Methods section and Supplementary Note 1 for details on sample fabrication and characterizations).

The measured representative near-field modes in the near-infrared to visible range are shown in Fig. 2a, c, with x-polarization at

normal incidence. In Fig. 2a, within the energy range from 1.03 eV (1200 nm) to 1.38 eV (900 nm), hyperbolic modes were clearly observed, with up to six distinct interference fringes visible (the bright points correspond to Au nanoparticles). The corresponding IFCs in Fig. 2b, obtained via fast Fourier transform (FFT) of Fig. 2a are well fitted by hyperbolic equations: $\frac{k_x^2}{\varepsilon_{y\_fit}} + \frac{k_y^2}{\varepsilon_{x\_fit}} = \omega^2/c^2$. The open angle decreases with increasing wavelength in k space, in agreement with calculations from the measured permittivity $\theta = \frac{\pi}{2} - \arctan\sqrt{-\varepsilon_x/\varepsilon_y}$ (Fig. 2f) (see Supplementary Note 5 for FFT data processing details). It should be noted that the observed maximum k is ~ 4k_O (Fig. 2b), significantly larger than the conventional Au SPPs (~ k_O)[27].

At shorter wavelengths with x-polarization, the hyperbolic mode becomes not observable anymore, whereas the elliptical air mode still emerges (Fig. 2c, d), with the transition occurring at ~ 1.77 eV (700 nm) (It should be noted that we can still observe 1 – 2 fringes of hyperbolic modes at 700 nm, but the visibility is very weak compared to that around 1000 nm). We attribute this transition to several possible reasons. First, as the wavelength decreases, the absorption of MoOCl$_2$
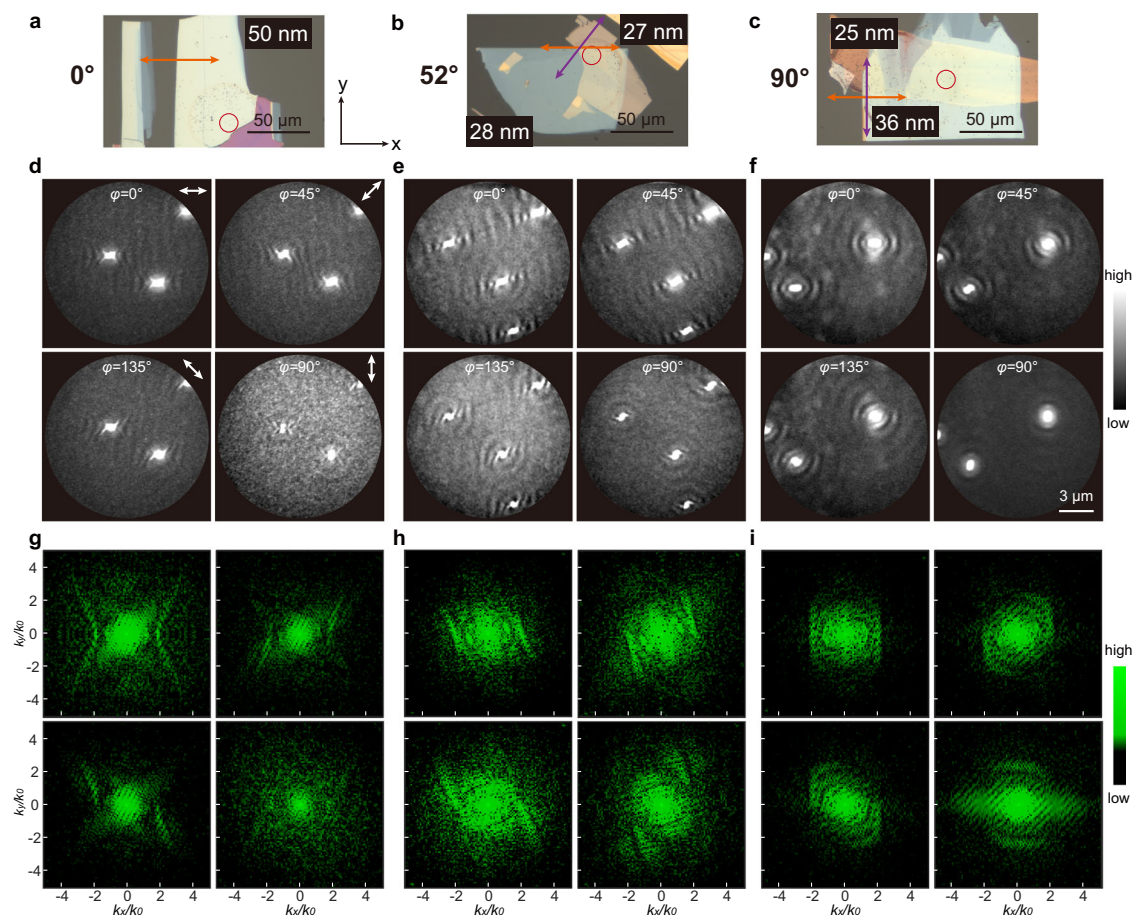
Fig. 3 | Polarization control in real and k spaces. a–c Optical images of MoOCl$_2$ samples with single flake and twisted bilayers. Thickness, twist angle, and PEEM measured area (red circle) are indicated. The arrows in (a–c) indicate the a-axis of MoOCl$_2$ flakes, and the flake with the orange arrow is below the flake with the purple arrow. d–i Corresponding PEEM and FFT images with the four polarizations at a representative wavelength of 1000 nm ($\varphi = 0°$ corresponds to x-polarization).

increases, leading to an increased loss for hyperbolic modes. Second, the real part of ε_x increases as wavelength decreases, indicating a weakening of the material's metallic properties and, consequently, diminishing the hyperbolic properties. Third, the excitation efficiency of the air mode is correlated with the size of the Au nanoparticle and increases with decreasing wavelength. At even shorter wavelengths (< 520 nm), no mode patterns are observed due to significant absorption losses. Our results indicate that MoOCl$_2$ has better plasmonic properties at longer wavelengths (e.g., > 800 nm) in the near-infrared than at shorter wavelengths (e.g., < 700 nm), which seems reasonable considering that even for conventional material Au is limited to work above ~ 600 nm in SPP excitations[35,41], and they have similar color under optical microscope. The enhanced absorption at shorter wavelengths originates from the d-band excitation in Au[42], whereas the case in MoOCl$_2$ is more complex, involving the total contribution of eight bands near the Fermi level, mainly from the 4d orbitals of Mo atoms[17].

The experimental results described above are well reproduced by simulations and theoretical calculations using the measured permittivity (See Supplementary Figs. 5–7 and further discussions on mode analysis in the Supplementary Note 7, including hyperbolic and air modes, as well as the lenticular mode, the latter of which can be significantly excited at short wavelengths with y-polarization). In addition, wavelength-dependent PEEM studies on a straight sample edge (along the y-axis) with x-polarization, along with the extracted dispersion relations, are presented in the Supplementary. Note 7 (Supplementary Fig. 8). The effect of MoOCl$_2$ flake thickness on the excited hyperbolic modes (Supplementary Fig. 10) and the inefficient

excitation with Au nanoparticles underneath MoOCl$_2$ (Supplementary Fig. 16) were also explored.

Polarization control and reconstruction of IFCs
To further characterize and manipulate the anisotropic behavior of hyperbolic plasmon polaritons, polarization control was performed for both single MoOCl$_2$ flakes and twisted bilayers (tBLs). For a single flake, as shown in Fig. 3a, the hyperbolic polaritons can be tailored by laser polarization. In real space (Fig. 3d), the propagation direction of hyperbolic modes changes with the rotation of light polarization, that is, the two branches of the hyperbola are excited asymmetrically. Such an asymmetry is more clearly observed in the k space (Fig. 3g), indicating polarization-selective excitation in the IFCs.

In the case of MoOCl$_2$ tBLs, the hyperbolic modes of the upper and lower layers hybridize, giving rise to new hybridized IFCs. The twist angle between the two layers offers a degree of control over polaritons, as already demonstrated in α-MoO$_3$[43–45]. Similar to the behavior in a single flake, laser polarization serves as an effective tool for controlling polaritons due to polarization-selective excitation in the hybridized IFCs. Fig. 3b, c showcase two representative samples with twist angles of approximately 52° and 90°, highlighting polarization control in a twisted system (see Supplementary Figs. 11 and 12 for the hyperbolic modes in each layer forming the tBLs). At a 52° twist, x-polarization results in directional propagation (Fig. 3e) and nearly flat IFCs (Fig. 3h), with this directionality further enhanced at 45°-polarization to the flatter IFCs, and reduced at 135°-polarization. At a 90° twist, an elliptical mode emerges in real space (Fig. 3f), signifying a topological transition induced by the twist angle, with the elliptical
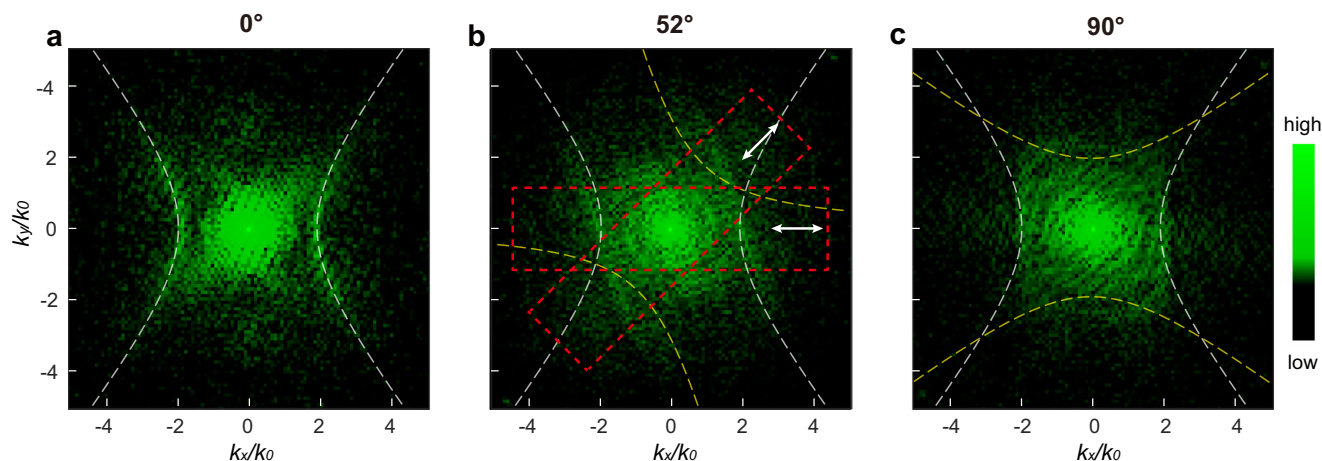
Fig. 4 | Reconstructed full IFCs. a–c Reconstructed IFCs by the superposition of the IFCs excited from the four representative polarizations in Fig. 3g–i. The principle of polarization-selective excitation in the IFCs is presented in (**b**), with the red dashed regions indicating the excitation range under specific polarizations. The white and yellow dashed lines correspond to the IFCs of the lower and upper layers of $MoOCl_2$, respectively.

mode rotating alongside the polarization. More importantly, at the 90° twist, the polarization selectivity in k space reveals rotating, square-like IFCs (Fig. 3i), suggesting the potential for using polarization excitations to reconstruct the full IFCs in k space.

As illustrated in Fig. 4, the full IFCs are reconstructed by combining the IFCs from the four representative polarization excitations shown in Fig. 3g–i. The range of observable IFCs is significantly expanded for tBLs, particularly at the 90° twist. It's important to note that at least two orthogonal polarizations are necessary to reconstruct the full IFCs. While using additional polarizations can improve the signal-to-noise ratio (see Supplementary Figs. 13 and 14 and Supplementary Movie. 1), the four representative polarizations in Fig. 3 are sufficient to achieve an acceptable signal quality. The polarization control in PEEM is effective and flexible, rather than by rotating the sample[46,47], which unprecedentedly revealed the full IFCs in the near-infrared and provided guidance for the manipulation of polaritons in applications.

Manipulating polaritons with artificial structures

The PEEM measurements discussed above are based on single-point excitation. However, for technological applications, fabricating artificial structures to control hyperbolic polaritons is a more practical approach[48,49]. In this study, we demonstrated the ability to manipulate polaritons using etched ring slits on $MoOCl_2$ (Fig. 5a, b). These ring slits act as point-array excitations, following Huygens' principle[50], as illustrated in Fig. 5c. The slits with predefined ring diameters (*d*) and slit widths (*w*) were fabricated using a focused ion beam (FIB). Representative PEEM images of a ring slit (*d* = 10 μm; *w* = 25 nm) at different wavelengths and x-polarization are presented in Fig. 5b. Both the variation in internal propagation patterns and external nanofocusing with changing wavelength can be observed, which aligns with the schematics provided in real and k spaces in Fig. 5c, d.

Hyperbolic polaritons offer the potential for superior nanofocusing compared to conventional SPPs, as they support much higher *k*-values, allowing them to surpass the diffraction limit. Polarization control of the hyperbolic mode was also demonstrated using ring slits to manipulate polariton propagation and focusing (Fig. 5e, f), highlighting their potential use in practical devices. In addition, the excitation efficiencies of hyperbolic polaritons with varying slit widths are explored in Supplementary Fig. 15. PEEM can further be utilized to characterize and detect more complex structures and devices on $MoOCl_2$, aiding in the optimization of their performance.

In summary, we have experimentally revealed the broadband near-infrared hyperbolic plasmon polaritons supported by $MoOCl_2$ flakes with the ultrahigh-spatial-resolution PEEM. The polaritons were dynamically tailored and controlled through tunable light polarization, wavelength at normal incidence and interlayer twist, observed in both real and k spaces. Particularly, the full iso-frequency contours were reconstructed by incorporating polarization-selective excitations. In addition, we demonstrated the feasibility to manipulate polaritons using designed artificial structures on $MoOCl_2$. This study also highlights PEEM as a highly effective method for nanoimaging polaritons in vdW materials, offering significant potential for nanoscale light manipulation. We believe that this work will stimulate broad interest in hyperbolic physics and its applications, including hyperbolic topological photonics, hyperbolic LSPRs, and hyperbolic polarization and sensing devices.

Methods

Sample fabrication and characterizations

The $MoOCl_2$ flakes were mechanically exfoliated on polydimethylsiloxane (PDMS) sheets from bulk crystals (Nanjing MKNANO Tech. Co., Ltd. (www.mukenano.com)), and the thicknesses of the $MoOCl_2$ flakes were estimated from the reflected color under optical microscopy and verified by atomic force microscopy (AFM). The selected $MoOCl_2$ flakes were transferred onto the soda-lime glass or silica glass substrate with ~ 10 nm ITO layer, by using the all-dry transfer method under optical microscopy. The transferred $MoOCl_2$ flakes were then covered with sparse SiO_2-coated Au nanoparticles (5 nm SiO_2 @ 200 nm Au, Nanjing/Jiangsu XFNANO Materials Tech Co., Ltd) or etched with a series of nanostructures by using focused ion beam (FIB). The 5 nm SiO_2 shell was used to reduce the photoemission intensity of bare Au nanoparticles, which is an essential trick for successful PEEM experiments. We also tested samples with 100 nm Au nanocubes or 200 nm Au nanoparticles underneath $MoOCl_2$ flakes. The characterizations of samples include optical images, scanning electron microscopy (SEM) images and AFM measurements. All samples were annealed under an ultrahigh vacuum (approximately 10^{-9} Torr) at 120 °C for 20 min before being loaded into the PEEM main chamber.

PEEM measurements

The PEEM measurements were performed on a high-resolution low-energy electron microscopy (LEEM)/PEEM system (ACSPELEEM III, Elmitec GmbH). A commercial Ti:sapphire femtosecond laser (Mai Tai HP, Spectra-Physics, pulse duration: 80 – 100 fs) operated at 690 – 1040 nm (2.9 W @ 820 nm) with a repetition rate of 80 MHz and an optical parametric oscillator (OPO) (Inspire Auto 100, Spectra-Physics, second harmonic generation (SHG) port: ~ 360 – 500 nm, signal port: ~ 490 – 750 nm, idle port: ~ 930 – 1800 nm) were used to provide a tunable laser (~ 360 – 1800 nm) for PEEM measurements.
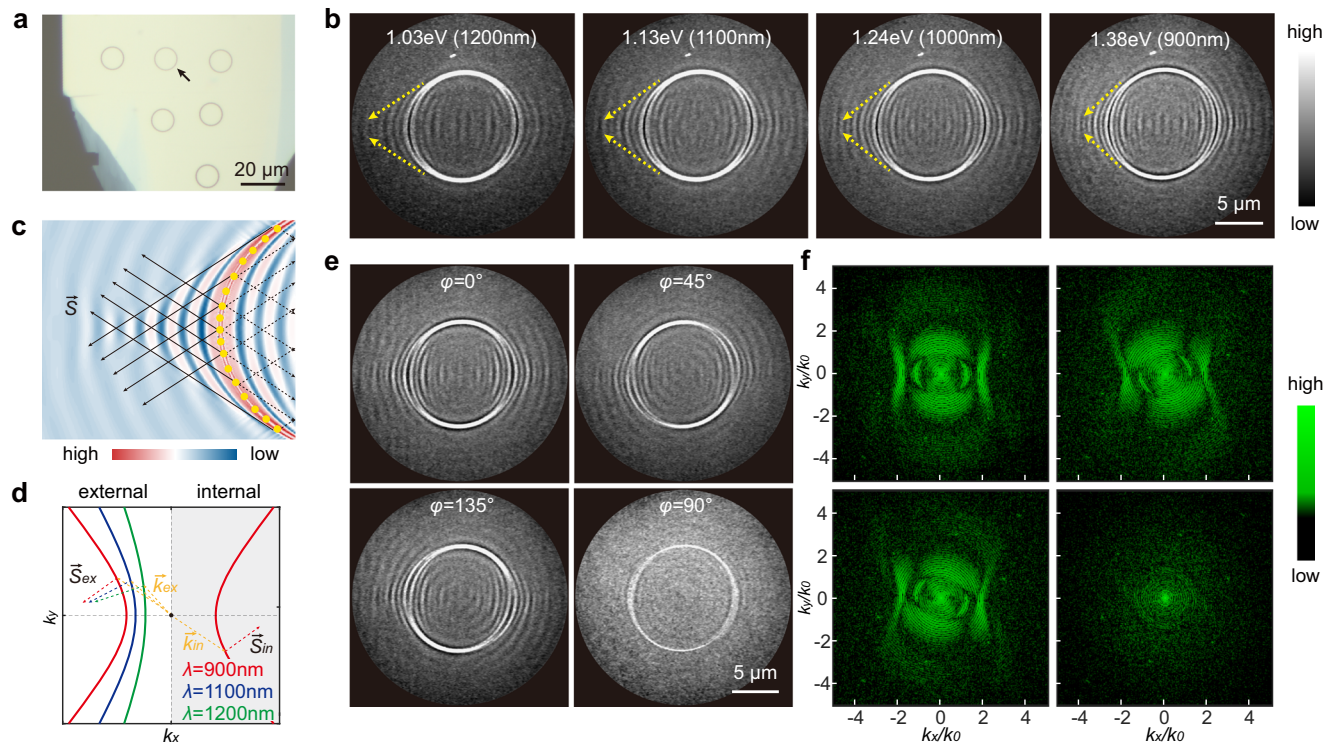
Fig. 5 | Manipulation of hyperbolic polaritons with artificial structures.
a Optical image of a representative MoOCl$_2$ flake (~ 60 nm) with etched ring slits.
b PEEM images at different wavelengths with x-polarization at normal incidence, for the ring slit marked in (**a**). The yellow dashed lines indicate the focusing of hyperbolic polaritons outside the ring slit. **c**, **d** Schematics of internal propagation and external nanofocusing induced by the curvature of ring slit in real and k spaces, respectively. In (**c**), the colors indicate the electric field intensity (low in blue and high in red). **e**, **f** Polarization control for another ring slit on a ~ 50 nm MoOCl$_2$ flake in real and k spaces, respectively.

The pulses were focused on the sample surface at normal incidence with a spot diameter of approximately 100 μm. The polarization of the laser is controlled by a λ/2 waveplate. A sub-monolayer of cesium (Cs) was deposited on the sample surface, reducing the work function to facilitate the two-photon photoemission process. All PEEM measurements were performed at ~ 85 K (liquid nitrogen cooling) to achieve better Cs deposition.

Simulations

The experimental results for MoOCl$_2$ excited by Au nanoparticles were well reproduced by finite-difference time-domain simulations using the measured permittivity. In the simulations, a 40 nm MoOCl$_2$ flake was used on a 10 nm ITO layer and glass substrate, with an Au nanoparticle (5 nm SiO$_2$ coated 200 nm Au sphere) on top of the MoOCl$_2$ flake. The in-plane refractive index of MoOCl$_2$ was obtained from our measurements. The excitation light was set to normal incidence with x- or y-polarization.

Data availability

The data supporting the findings are displayed in the main text and the Supplementary Information. All raw data are available from the corresponding authors upon request.

Code availability

Codes supporting the results of this work are available from the corresponding authors upon request.

References

1. Zhang, Q. et al. Interface nano-optics with van der Waals polaritons. *Nature* **597**, 187–195 (2021).
2. Wu, Y. et al. Manipulating polaritons at the extreme scale in van der Waals materials. *Nat. Rev. Phys.* **4**, 578–594 (2022).
3. Dai, S. et al. Tunable phonon polaritons in atomically thin van der waals crystals of boron nitride. *Science* **343**, 1125–1129 (2014).
4. Sternbach, A. J. et al. Negative refraction in hyperbolic hetero-bicrystals. *Science* **379**, 555–557 (2023).
5. Ma, W. et al. In-plane anisotropic and ultra-low-loss polaritons in a natural van der Waals crystal. *Nature* **562**, 557–562 (2018).
6. Zheng, Z. et al. A mid-infrared biaxial hyperbolic van der Waals crystal. *Sci. Adv.* **5**, eaav8690 (2019).
7. Taboada-Gutiérrez, J. et al. Broad spectral tuning of ultra-low-loss polaritons in a van der Waals crystal by intercalation. *Nat. Mater.* **19**, 964–968 (2020).
8. Ma, W. et al. Ghost hyperbolic surface polaritons in bulk anisotropic crystals. *Nature* **596**, 362–366 (2021).
9. Basov, D. N., Fogler, M. M. & García de Abajo, F. J. Polaritons in van der Waals materials. *Science* **354**, aag1992 (2016).
10. Galiffi, E. et al. Extreme light confinement and control in low-symmetry phonon-polaritonic crystals. *Nat. Rev. Mater.* **9**, 9–28 (2024).
11. Hu, F. et al. Imaging exciton–polariton transport in MoSe$_2$ waveguides. *Nat. Photonics* **11**, 356–360 (2017).
12. Luo, Y. et al. Electrically switchable anisotropic polariton propagation in a ferroelectric van der Waals semiconductor. *Nat. Nanotechnol.* **18**, 350–356 (2023).
13. Wang, T. et al. Magnetically-dressed CrSBr exciton-polaritons in ultrastrong coupling regime. *Nat. Commun.* **14**, 5966 (2023).
14. Wu, J.-S., Basov, D. & Fogler, M. Topological insulators are tunable waveguides for hyperbolic polaritons. *Phys. Rev. B* **92**, 205430 (2015).
15. Ni, G. X. et al. Fundamental limits to graphene plasmonics. *Nature* **557**, 530–533 (2018).
16. Zhao, J. et al. Highly anisotropic two-dimensional metal in monolayer MoOCl$_2$. *Phys. Rev. B* **102**, 245419 (2020).

17. Gao, H., Ding, C., Sun, L., Ma, X. & Zhao, M. Robust broadband directional plasmons in a MoOCl$_2$ monolayer. *Phys. Rev. B* **104**, 205424 (2021).

18. Fang, Y., Wang, F., Wang, R., Zhai, T. & Huang, F. 2D NbOI$_2$: a chiral semiconductor with highly in-plane anisotropic electrical and optical properties. *Adv. Mater.* **33**, 2101505 (2021).

19. Abdelwahab, I. et al. Giant second-harmonic generation in ferroelectric NbOI$_2$. *Nat. Photonics* **16**, 644–650 (2022).

20. Guo, Q. et al. Ultrathin quantum light source with van der Waals NbOCl$_2$ crystal. *Nature* **613**, 53–59 (2023).

21. Gao, H. et al. Broadband type-I hyperbolicity independent of carrier density in RuOCl$_2$ crystals. *Phys. Rev. B* **109**, 115432 (2024).

22. Venturi, G., Mancini, A., Melchioni, N., Chiodini, S. & Ambrosio, A. Visible-frequency hyperbolic plasmon polaritons in a natural van der Waals crystal. *Nat. Commun.* **15**, 9727 (2024).

23. Ruta, F. L. et al. Good plasmons in a bad metal. *Science* **387**, 786–791 (2025).

24. Kahl, P. et al. Normal-incidence photoemission electron microscopy (NI-PEEM) for imaging surface plasmon polaritons. *Plasmonics* **9**, 1401–1407 (2014).

25. Dabrowski, M., Dai, Y. & Petek, H. Ultrafast photoemission electron microscopy: imaging plasmons in space and time. *Chem. Rev.* **120**, 6247–6287 (2020).

26. Kubo, A., Pontius, N. & Petek, H. Femtosecond microscopy of surface plasmon polariton wave packet evolution at the silver/vacuum interface. *Nano Lett.* **7**, 470–475 (2007).

27. Spektor, G. et al. Revealing the subfemtosecond dynamics of orbital angular momentum in nanoplasmonic vortices. *Science* **355**, 1187–1191 (2017).

28. Davis, T. J. et al. Ultrafast vector imaging of plasmonic skyrmion dynamics with deep subwavelength resolution. *Science* **368**, eaba6415 (2020).

29. Dai, Y. et al. Plasmonic topological quasiparticle on the nanometre and femtosecond scales. *Nature* **588**, 616–619 (2020).

30. Hartelt, M. et al. Energy and momentum distribution of surface plasmon-induced hot carriers isolated via spatiotemporal separation. *ACS nano* **15**, 19559–19569 (2021).

31. Sun, Q., Zu, S. & Misawa, H. Ultrafast photoemission electron microscopy: Capability and potential in probing plasmonic nanostructures from multiple domains. *J. Chem. Phys.* **153**, 120902 (2020).

32. Kubo, A. et al. Femtosecond imaging of surface plasmon dynamics in a nanostructured silver film. *Nano Lett.* **5**, 1123–1127 (2005).

33. Sun, Q. et al. Direct imaging of the near field and dynamics of surface plasmon resonance on gold nanostructures using photoemission electron microscopy. *Light. Sci. Appl.* **2**, e118 (2013).

34. Sun, Q. et al. Dissecting the few-femtosecond dephasing time of dipole and quadrupole modes in gold nanoparticles using polarized photoemission electron microscopy. *ACS Nano* **10**, 3835–3842 (2016).

35. Li, Y. et al. Correlation between near-field enhancement and dephasing time in plasmonic dimers. *Phys. Rev. Lett.* **124**, 163901 (2020).

36. Pres, S. et al. Detection of a plasmon-polariton quantum wave packet. *Nat. Phys.* **19**, 656–662 (2023).

37. Fitzgerald, J., Word, R. C., Saliba, S. & Könenkamp, R. Photonic near-field imaging in multiphoton photoemission electron microscopy. *Phys. Rev. B* **87**, 205419 (2013).

38. Fitzgerald, J., Word, R. C. & Könenkamp, R. Subwavelength visualization of light in thin film waveguides with photoelectrons. *Phys. Rev. B* **89**, 195129 (2014).

39. Liu, W. et al. Imaging and controlling photonic modes in perovskite microcavities. *Adv. Mater.* **33**, 2100775 (2021).

40. Li, Y. et al. Revealing low-loss dielectric near-field modes of hexagonal boron nitride by photoemission electron microscopy. *Nat. Commun.* **14**, 4837 (2023).

41. Sönnichsen, C. et al. Drastic reduction of plasmon damping in gold nanorods. *Phys. Rev. Lett.* **88**, 077402 (2002).

42. Amendola, V., Pilot, R., Frasconi, M., Maragò, O. M. & Iatì, M. A. Surface plasmon resonance in gold nanoparticles: a review. *J. Phys. Condens. matter* **29**, 203002 (2017).

43. Hu, G. et al. Topological polaritons and photonic magic angles in twisted α-MoO$_3$ bilayers. *Nature* **582**, 209–221 (2020).

44. Chen, M. Y. et al. Configurable phonon polaritons in twisted α-MoO$_3$. *Nat. Mater.* **19**, 1307–1311 (2020).

45. Hu, G., Krasnok, A., Mazor, Y., Qiu, C.-W. & Alù, A. Moiré hyperbolic metasurfaces. *Nano Lett.* **20**, 3217–3224 (2020).

46. Hu, C. et al. Source-configured symmetry-broken hyperbolic polaritons. *eLight* **3**, 14 (2023).

47. Hu, G. et al. Real-space nanoimaging of hyperbolic shear polaritons in a monoclinic crystal. *Nat. Nanotechnol.* **18**, 64–70 (2023).

48. Duan, J. et al. Planar refraction and lensing of highly confined polaritons in anisotropic media. *Nat. Commun.* **12**, 4325 (2021).

49. Álvarez-Pérez, G. et al. Negative reflection of nanoscale-confined polaritons in a low-loss natural medium. *Sci. Adv.* **8**, eabp8486 (2022).

50. Martín-Sánchez, J. et al. Focusing of in-plane hyperbolic polaritons in van der Waals crystals with tailored infrared nanoantennas. *Sci. Adv.* **7**, eabj0127 (2021).

Acknowledgements

Author contributions

Q.G., X.H., G.L., and S.W. hosted the project. Y.Li and Z. Chen conceived the idea. Y.Li, Y.Z., J. X., X.Li, P.J., J.T., Q.Lyu, Y.Luo and Z. Cao conducted the PEEM experiments. Y.Li, and Y.Z. conducted data analyses and simulations. Y.Li., G.Z., X.Liao, Y.T. and R.Y. conducted the sample preparations. Y.Li, Y.Z. and Q.Liu conducted the sample characterizations. W.Z. and W.L. conducted the refractive index measurements. H.Y., Q.S., Y.G., S.W., P.W. and M.A. contribute to the data analyses and explanations. All authors contributed to writing the original draft, reviewing, and editing.

Competing interests

The authors declare no competing interests.

Additional information